



Optimization of the IO₃ polar group of BiOIO₃ by bulk phase doping amplifies pyroelectric polarization to enhance carrier separation and improve the pyro-photo-electric catalytic performance

Yunfei Wu ^a, Mengnan Ruan ^{a,b}, Zhengang Guo ^{a,b}, Chengyi Wang ^{a,b}, Zhifeng Liu ^{a,b,*}

^a School of Materials Science and Engineering, Tianjin Chengjian University, 300384 Tianjin, China

^b Tianjin Key Laboratory of Building Green Functional Materials, Tianjin Chengjian University, 300384 Tianjin, China



ARTICLE INFO

Keywords:

BiOIO₃

Polar group

N-doping

Pyroelectric

Pyro-photo-electric catalysis

ABSTRACT

The internal polarization field generated by spontaneous polarization of pyroelectric materials is an effective means of separating electrons and holes in the pyroelectric catalysis. And the polar group is the key to the intensity of material polarization. In this paper, the effect of the introduction of polar groups by N on the pyro-photo-electric catalytic performance of the BiOIO₃ is investigated for the first time and the mechanism of action is analyzed. The current density of the N introduced BiOIO₃ photoanode reached up to 0.108 $\mu\text{A cm}^{-2}$ at 1.23 V vs. RHE under the excitation of temperature change, which is twice as high as that of the bare BiOIO₃. The current density is further increased to a maximum value of 0.187 $\mu\text{A cm}^{-2}$ at 1.23 V vs. RHE after the introduction of light. Detailed experimental studies and theoretical calculations show that the substitution of O at the V3 position in the polar group of IO₃ by an N atom results in a change in the polar structure. This change not only amplifies the internal polarization field and thus promotes carrier separation, but also optimizes the pyro-photo-electric catalytic efficiency. This way of direct action on the polar group provides reference for further studies on the macroscopic polarization of polar materials and offers optimization idea for the field of pyro-photo-electric catalysis.

1. Introduction

In recent years, energy and environmental problems in the world have attracted much attention [1,2]. Solving energy problems is the basis for ensuring normal production and life, and environmental problems have an important impact on future development. Hydrogen energy [3] as an efficient, environmentally friendly energy carrier and has attracted widespread attention. As a renewable energy source, solar energy [4] is green, non-polluting and never depleting, which is an important direction for global energy transition. Among the hydrogen production methods that have been studied, hydrogen production by photoelectrochemical (PEC) water splitting using semiconductor materials is considered to be the most efficient way to produce hydrogen due to its unique advantages [5]. So far, researchers have intensively explored various semiconductor materials such as TiO₂ [6,7], ZnO [8,9], CdS [10,11], Fe₂O₃ [12,13] and BiVO₄ [14–16]. However, the wide forbidden band width makes the optical utilization of semiconductors low, and in addition low carrier separation and high carrier

complexation are still important problems plaguing PEC technology. For this reason, various modifications have been carried out for semiconductor materials, including structure optimization [17,18], construction of heterojunctions [19–21], doping [22–24] and co-catalysts [25]. However, the carrier separation efficiency of the modified semiconductors still fails to meet scientific expectations. Therefore, it is particularly important to explore new catalytic strategies to improve the carrier transport.

Temperature variation [26] is a clean and abundant form of energy that originates from nuclear power plants, thermal power plants and other forms of industrial waste heat as well as diurnal temperature variations, and is a common phenomenon in production life. Therefore, using solar energy, industrial waste heat, etc. and converting them into chemical energy is a potential strategy, and utilizing these renewable energy sources provides a solution to the deteriorating environmental problems and the expanding energy demand. Therefore, pyroelectric materials [27] have attracted a lot of attention because of their unique polarization advantages. Pyroelectricity can be explained by the fact

* Corresponding author at: School of Materials Science and Engineering, Tianjin Chengjian University, 300384 Tianjin, China.

E-mail address: tjulzf@163.com (Z. Liu).

that certain highly asymmetric crystals exhibit spontaneous polarization and eventually current and potential changes with temperature changes. Pyroelectric nanomaterials [28] are more suitable than other materials for converting thermal energy into chemical energy because such materials require only temporal temperature gradient (dT/dt) and are almost independent of the spatial environment. Including LiNbO_3 [29], BaTiO_3 [30], CdS [31,32], BiOIO_3 [33] and NaNbO_3 [34] are all pyroelectric materials. In recent years, pyroelectric catalysis, which combines pyroelectric effects and redox reactions, has been investigated and applied to pyro-photo-electric catalysis (pyro-PEC). For example, Li et al. designed a 2D ultrathin Co(OH)_2 nanosphere layer on NaNbO_3 [35]. The synergistic effect of pyroelectric effect and surface reaction kinetics optimization greatly improved the transport kinetics of photo/pyrolytic carriers. The fabricated $\text{NaNbO}_3/\text{Co(OH)}_2$ composite photoanode exhibited a high current density of 1.68 mA cm^{-2} under the stimulation of light and cold-hot cycles, which was 2.63 times higher than that before the modification. Thus pyro-PEC is a reliable strategy to improve the catalytic performance of semiconductors. Among the various pyroelectric materials, orthorhombic system BiOIO_3 [36] is a layered bismuth-based Aurivillius compound consisting of alternating $(\text{Bi}_2\text{O}_2)^{2+}$ layers and polar $(\text{IO}_3)^-$ polyhedral. The special layered structure provides carrier transport channels and the polar $(\text{IO}_3)^-$ polyhedral make the pyroelectric catalysis of BiOIO_3 possible. So far, it has been demonstrated that the internal polar field generated by spontaneous polarization of BiOIO_3 can be used for hydrogen evolution reactions, and the internal polar field effect can promote carrier separation [37]. Therefore, amplification of pyroelectric polarization by appropriate modification approach is expected to improve the pyroelectrocatalytic performance of BiOIO_3 , and the performance may be further improved by combining pyroelectrocatalysis and photoelectrocatalysis. However, to the best of our knowledge there are no relevant reports on the optimization of BiOIO_3 polarization groups for pyro-PEC.

Here, we investigated the effect of detail optimization of polar group on the pyroelectric polarization and pyro-PEC performance of the material. The effect of the introduction of N atoms on the polarization level of BiOIO_3 was explored by successfully replacing the O atoms in the IO_3 pyramid by introducing N atoms into the pyramid, thus changing the polarization environment and revealing the connection with the pyro-PEC activity. The introduction of N not only enhances the pyroelectric polarization but also strengthens the internal polarization field, which facilitates carrier separation. This work discusses a method to explore the polarization properties of BiOIO_3 by optimizing the structure of polar groups through elemental doping and provides an effective scheme for the integrated use of thermal, optical and electrical energy.

2. Experimental section

2.1. Preparation of sample

All chemicals in the experimental procedure were of analytical grade and no further purification was required. The F-doped tin oxide conductive glass was sonicated for 15 min using anhydrous ethanol, acetone, and isopropanol, respectively, and dried for use. Solution A was obtained by first dissolving 1 mmol $\text{Bi}(\text{NO}_3)_3 \cdot 5 \text{ H}_2\text{O}$ in 40 ml of deionized water and stirring vigorously on a magnetic stirrer until a milky suspension was formed. Solution B was obtained by mixing 1 mmol KIO_3 with 20 ml of deionized water. Solution B was added to solution A with continuous stirring after KIO_3 was completely dissolved. During stirring, 1 ml of concentrated HNO_3 at 67% (w/w) and 1 ml of NaOH at 2.0 M were added drop by drop to the mixed turbid solution to obtain the precursor solution. The precursor solution was placed in a 100 ml Teflon-lined stainless-steel autoclave at 150 °C for 10 h and then cooled to room temperature. The BiOIO_3 samples were obtained after centrifugation with deionized water and ethanol three times, respectively, and dried at 60 °C for 12 h. The $\text{BiOIO}_3\text{-N}_x$ samples were obtained by mixing 0.2 g of BiOIO_3 with different levels of urea (0.02 g, 0.06 g, 0.1 g) and

then annealing in a muffle furnace at 300 °C for 3 h. The mass ratios of urea to BiOIO_3 were 1:10, 3:10 and 5:10, respectively. The $\text{BiOIO}_3\text{-N}_x$ samples were recorded as $\text{BiO-N}_{0.1}$, $\text{BiO-N}_{0.3}$ and $\text{BiO-N}_{0.5}$, respectively. 100 μL of Nafion solution and 2 ml of isopropanol were added to 0.05 g of $\text{BiOIO}_3\text{-N}$ sample, and then the mixture was sonicated for 20 min. The mixed solution was applied to the FTO glass substrate using a pipette gun and dried at room temperature for 12 h to obtain the working electrode.

2.2. Characterization

The phase composition of the samples was analyzed using X-ray diffractometry (XRD, Rigaku-D/max-2500, Cu $\text{K}\alpha$ radiation) and compared with standard cards. Scanning electron microscopy (SEM, JEOL JSM-7800 F) and energy spectrometry (EDS) and X-ray photoelectron spectroscopy (XPS, Thermo ESCALAB 250XI, Al- $\text{K}\alpha$ X-ray) were used to study the microscopic morphological characteristics, elemental composition and distribution of the samples. Transmission electron microscopy (Tecnai G2 Model 20) and high-resolution electron microscopy (HRTEM) were used to observe the morphological and lattice information of the samples. The spectral response range of the samples was recorded using a DU-8B UV-Vis spectrophotometer (UV-Vis), from which the optical band gap energy of the samples could be calculated as follows:

$$E_g = 1240 / \lambda_{\text{Absorp}} \quad \text{Edge} \quad (1)$$

$$a\hbar\nu = A(\hbar\nu - E_g)^{n/2} \quad (2)$$

where A is a constant, α , $\hbar\nu$ and E_g are the absorption coefficients, photon energy and band gap energy, respectively. Where n depends on the optical leap form of the semiconductor ($n = 1$ for direct leap and $n = 4$ for indirect leap), BiOIO_3 belongs to indirect leap, so $n = 4$ [38]. In addition, charge separation kinetic information of the sample was obtained by surface photovoltage (SPV). The device was equipped with a 500 W xenon lamp as the light source, an SR830 lock-in amplifier, and a sample chamber and surface photovoltage spectrometer (PLSPS/IPCE1000). The charge complexation rate of the samples was examined using photoluminescence properties (PL), model OmniFluo 960 H-320PL.

2.3. Pyroelectrochemical and photoelectrochemical measurements

The pyroelectric and photoelectrochemical properties of the samples were evaluated using a constant potential electrochemical workstation (CHI760E, Changhua, Shanghai, China) with Ag/AgCl as reference electrode and platinum (Pt) sheet as counter electrode, using a 300 W xenon lamp to simulate a solar light source and a 1.5 G filter to control the light intensity at 100 mW cm^{-2} . The electrolyte was a 0.1 M Na_2SO_4 solution. Finally, the measured potential was converted into a reversible hydrogen electrode (RHE) using the Nernst equation [39]:

$$E_{\text{RHE}} = E_{\text{Ag/AgCl}} + 0.0591pH + 0.1976V \quad (3)$$

The current density-voltage (J-V) curves were measured by linear scanning voltammetry (LSV) from 0 V to 1.23 V_{RHE} at a scan rate of 10 mV s^{-1} . The electrochemical impedance spectra (EIS) were measured in the frequency range of 0.01 Hz-100 kHz and at an AC bias of 0.65 V at a scan rate of 20 mV s^{-1} . To obtain the flat-band potential of the samples, the EIS was measured in different environments at Mott-Schottky (M-S) curves with a frequency of 1000 Hz and an AC amplitude of 10 mV were measured [40]:

$$\frac{1}{c^2} = \frac{2}{\varepsilon \epsilon_0 e A^2 N_d} \left(V - V_{fb} - \frac{K_B T}{e} \right) \quad (4)$$

where C is the space charge capacitance, ε and ϵ_0 are the vacuum

dielectric constant and relative dielectric constant of BiOIO_3 , ϵ is the fundamental charge, A is the coated area of the working electrode (1 cm^2), N_d is the applied density, V is the applied bias voltage, and V_{fb} is the flat-band potential. K_B is the Boltzmann constant ($1.38 \times 10^{-23} \text{ J K}^{-1}$), and T is the temperature (K).

Applied bias photon to current efficiency (ABPE) can be calculated by the following equation, which is used to estimate the maximum photoconversion efficiency of the sample [41].

$$\text{ABPE} = (J_{\text{light}} - J_{\text{dark}}) \left(\frac{1.23 - V_{\text{RHE}}}{P_{\text{light}}} \right) \quad (5)$$

where J_{light} and J_{dark} are the photocurrent densities under light and dark conditions, V_{RHE} is the relationship between the applied potential and RHE, and P_{light} is the photo-radiometric intensity of the incident light (100 mW cm^{-2} , AM 1.5 G).

2.4. Calculation method

Structural optimization of the samples was carried out using Materials Studio software. Calculations and simulations are performed using CASTEP with the generalized gradient approximation with the Perdew-Burke-Ernzerhof (PBE) exchange and correlation functional. The calculation parameters were set to improve the accuracy of the optimization. These include limiting the plane wave energy to 500 eV, the k -point with a density of $(4 \times 2 \times 4)$ points in the Brillouin zone of the unit cell, setting the self-consistent-field energy convergence of 10^{-6} and allowing atomic relaxation.

3. Results and discussion

Firstly, the material phase composition and the degree of crystallinity of the materials were analyzed using XRD, and the BOI-N_x ($0.1 \leq x \leq 0.5$) powder diffractograms for BiOIO_3 as well as for different N contents after their introduction are shown in Fig. 1(a). The diffraction peaks of all samples are consistent with the ICSD No. 26–2019 standard card [42]. The peaks were high and sharp, with no peak packets and no cluttered peaks in the measurement range, indicating that the BiOIO_3 samples were successfully prepared and had good crystallinity. A slight peak shift phenomenon was observed after local magnification of the main peak (121). This may be due to the introduction of N atoms. According to the Bragg equation ($n\lambda = 2d\sin\theta$) [43], the smaller the value of 2θ , the larger the lattice spacing. The atomic radius of N atoms is slightly larger than that of O atoms, and the introduction of N increases the cell size of BiOIO_3 , which causes micro-strain. As a result, the substitution of O by N will shift the diffraction peak to a small angle. Therefore, the introduced N atom may replace the O atom in BiOIO_3 . The data also indicate that all samples after the introduction of N atoms have the same crystalline shape as BiOIO_3 , are in orthorhombic phase, and have space group Pca21 (29). The elemental composition and chemical states of BiOIO_3 and $\text{BOI-N}_{0.3}$ were subsequently analyzed using X-ray photo-electron spectroscopy (XPS). As shown in Fig. 1(c), the elements C, I, O, and Bi were detected in the BiOIO_3 sample. The complete XPS pattern is shown in Fig. S1, where element C is the intrinsic XPS calibration element [44]. The two peaks with binding energies of 623.5 eV and 635.1 eV correspond to $\text{I 3d}_{3/2}$ and $\text{I 3d}_{5/2}$ [45], respectively, and the two peaks with binding energies of 530.0 eV and 631.9 eV are attributed to O-H and Bi-O bonds [46], respectively. The two peaks at binding energies of 158.8 eV and 164.2 eV correspond to the $\text{Bi 4 f}_{7/2}$ and $\text{Bi 4 f}_{5/2}$

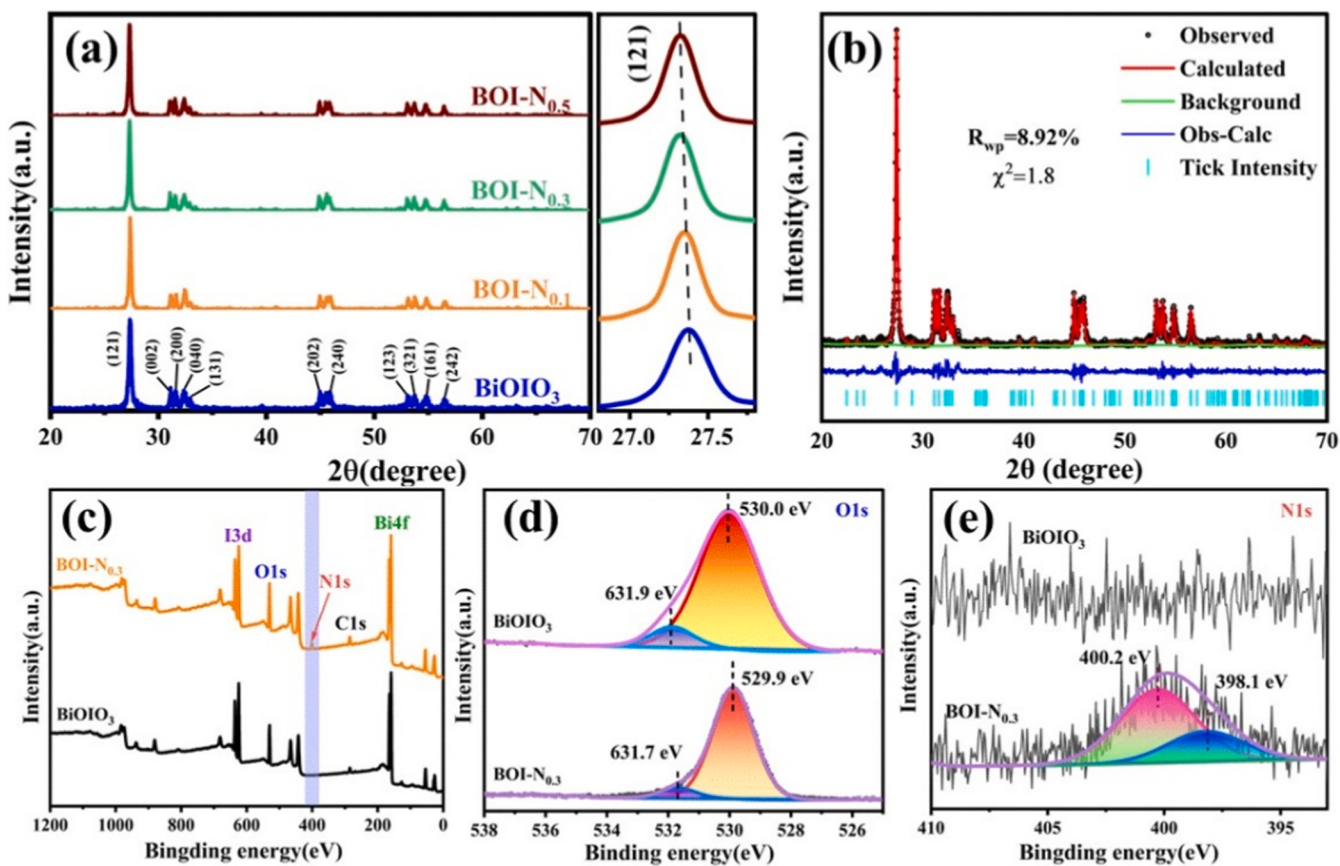


Fig. 1. (a) X-ray powder diffraction patterns of BiOIO_3 and BOI-N_x ($0.1 \leq x \leq 0.5$) samples. For comparison, the (121) peaks are enlarged on the right side; (b) X-ray powder diffraction pattern of $\text{BOI-N}_{0.3}$ sample was observed and calculated, and the Rietveld refinement convergence of the refinement result with good R and χ^2 values; (c), (d), (e) High-resolution XPS spectra of $\text{BOI-N}_{0.3}$ sample.

states [47], respectively. For the $\text{BOI-N}_{0.3}$ sample, the presence of N was detected in addition to the above elements. The characteristic peaks at 398.1 eV and 400.2 eV can be attributed to the N-Bi-O and N-O bonds [48], respectively. And the characteristic peaks of the other elements were shifted, indicating that N was successfully introduced into the lattice of BiOIO_3 . Fourier infrared spectroscopy (FT-IR) was performed on the samples to analyze the chemical bonding properties of the functional groups on the catalyst surface. As shown in Fig. S2, the vibrational peak of the Bi-O bond is located at 150.8 cm^{-1} . The two vibrational peaks of the I-O bond are located at 679.1 cm^{-1} and 770.4 cm^{-1} [49]. In addition, with the introduction of N atoms, a new peak is added compared to the pure BiOIO_3 , and the vibrational peak located at 1456.7 cm^{-1} comes from the stretching vibration of the N-O bond. Combined with the above analysis, it can be concluded that a certain amount of N element is introduced into the lattice of the BiOIO_3 matrix.

Scanning electron microscopy (SEM) images of BiOIO_3 and BOI-N_x ($0.1 \leq x \leq 0.5$) are given in the supporting information. Fig. S3 shows that all samples prepared are nanosheet morphologies, and the morphology of the samples after the introduction of N atoms does not change significantly. Therefore, the introduction of N atoms has no significant effect on the morphology of BiOIO_3 . To better observe the microscopic morphological information and elemental distribution of the samples, transmission electron microscopy (TEM) and high-resolution transmission electron microscopy images of $\text{BOI-N}_{0.3}$ were tested. Fig. 2(a), (b) shows that the sample morphology appears as nanosheets, which is in agreement with the SEM image results. In Fig. 2(d) we are fortunate to observe the slip of the lattice. The results show that the crystal face is a (050) crystal face and the angle of the lattice has changed after the lattice slip. According to the previous analysis, the lattice expands from 0.221 nm to 0.273 nm, which provides evidence for O-site substitution of N. Furthermore, the element mapping images in the Fig. 2(e) region (Fig. 2(f), (g), (h)) clearly show the element distribution in $\text{BOI-N}_{0.3}$, and it can be observed that in addition to I, O, and Bi elements N elements are also uniformly distributed on the sample surface. In addition, the corresponding EDX plots and elemental contents are included in Fig. S4.

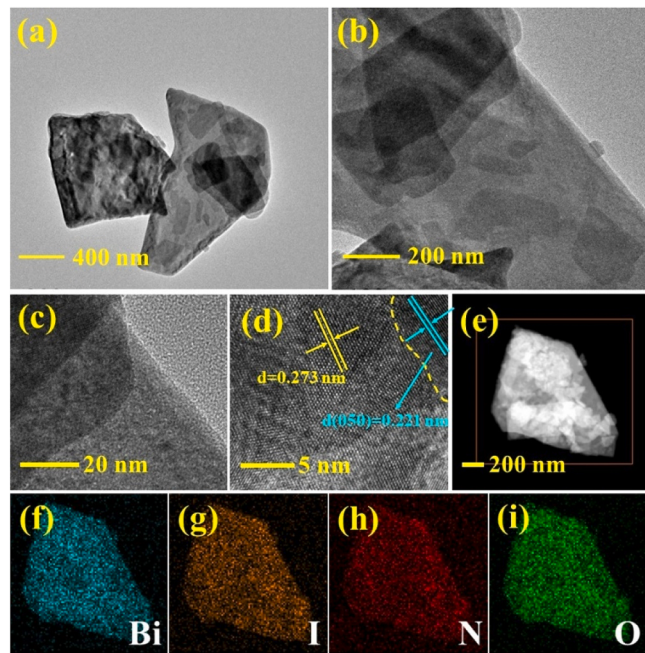


Fig. 2. (a), (b) TEM image and (c), (d) HRTEM images of $\text{BiOIO}_{0.3}$ sample; (e) STEM-EDX element mapping zone; and (f), (g), (h), (i) corresponding element mapping images of $\text{BOI-N}_{0.3}$ sample.

In order to elucidate the position of N atoms introduced in BiOIO_3 , we classified all the O in it into four categories according to the different states of O sites and labeled them as V1, V2, V3, and V4, respectively (Fig. 3). The total energy of the N atom substitution at different positions was calculated separately by density general function theory (DFT), and the results are summarized in Tab. S1. The results show that the N atom ends up with the lowest total energy when replacing O at position V3. The principle of lowest energy, introduced by the first law of thermodynamics, indicates the most stable structure. This also indicates that most of the N will replace the O at the V3 position after the introduction of N element into BiOIO_3 . Further, the XRD pattern of $\text{BOI-N}_{0.3}$ was refined by XRD using GSAS-II to obtain Fig. 1(b), where the black dots are the experimental values, the red curve is the simulated value, and the blue curve is the difference between the two. The data show that $\text{BOI-N}_{0.3}$ also belongs to the orthorhombic system Pca21(29) space group crystallization and the experimental and simulated results are in good agreement. The N and oxygen atoms coexist in the same position and the N content is 0.3122, which is in general agreement with the elemental content in STEM-EDX. More simulation results are presented in Tab. S2.

The UV-vis spectra can characterize the absorbance properties of the semiconductor very well. As shown in Fig. 4(a), it can be seen that the absorption edge is around 390 nm, while the absorption edge of the sample is continuously red-shifted with the increase of the N-source concentration of the precursor solution. It is noteworthy that the blue shift occurs at the addition of N source up to 0.1 g compared to the addition of 0.06 g. This may be due to the saturation of N adsorption by the sample and the negative effect of the excess N on the light absorption of the sample [50]. We then extrapolated the bandgap equation to zero absorption to obtain the bandgap energy of the sample and obtained the curve of $(\alpha h\nu)^{1/2}$ versus photon energy $h\nu$ and displayed in the inset of Fig. 4(a). As can be seen from the figure, the forbidden band widths of BiOIO_3 , $\text{BOI-N}_{0.1}$, $\text{BOI-N}_{0.3}$ and $\text{BOI-N}_{0.5}$ are 3.04 eV, 2.85 eV, 2.56 eV and 2.76 eV, respectively. this indicates that the introduction of N improves the light absorption of the catalyst and broadens the spectral absorption range. The introduction of impurity ions formed impurity energy levels in the forbidden band of BiOIO_3 , which facilitated the electron leap. Nevertheless, a large complex of electron-hole pairs was still observed in the photoluminescence spectrum (PL) [51]. As in Fig. 4 (b), the carrier complexation is larger before and after the modification, and the lowest complexation is observed for the $\text{BOI-N}_{0.3}$ sample in comparison. Therefore, the introduction of N element prolongs the complexation time of electrons and holes to some extent, but it is not the main factor for the performance improvement.

Subsequently, a series of tests were employed to evaluate the

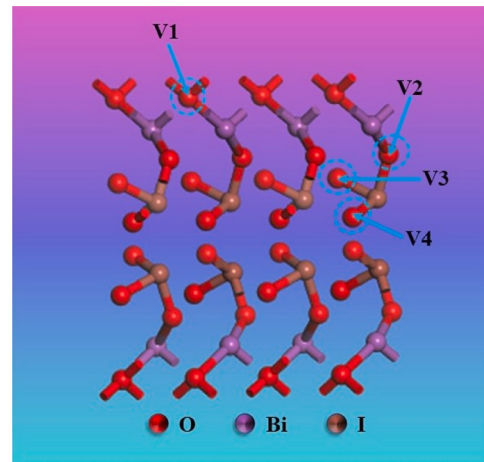


Fig. 3. Schematic diagram of the crystal structure of BiOIO_3 , with the purple, brown and red spheres representing the Bi, I and O atoms, respectively. (V1, V2, V3, V4) represent the different oxygen positions.

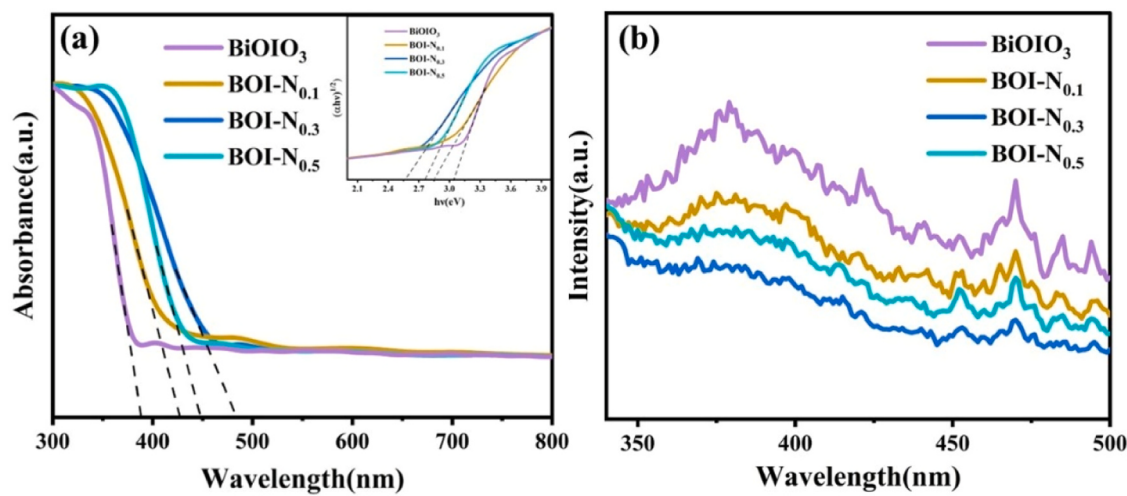


Fig. 4. (a) UV-vis absorption and the inset shows the corresponding Tauc plot of the samples; (b) Photoluminescence Spectra of BiOIO₃ and BOI-N_x ($0.1 \leq x \leq 0.5$) samples.

thermoelectric properties of the samples before and after modification. First, the thermoelectric properties of BiOIO₃ were verified by transient thermoelectric current tests. Specifically, the I-T curves of the samples were measured under cold-hot stimuli from 20 °C to 50 °C. The ideal temperature profile is shown in Fig. S5. As shown in Fig. 5, the current density after the temperature switch from 20 °C to 50 °C is suddenly enhanced and then slowly decreased. Similarly, there is a similar change in the current density after the temperature switch from 50 °C to 20 °C. This is due to the pyroelectric polarization property of BiOIO₃. When the external temperature changes, the polarization intensity of the catalyst changes, which enhances the current density, and after reaching the equilibrium the polarization charge is shielded leading to a decrease in the current density. The J-V curves of different samples under different environments are shown in Fig. 6(a), (b) and (c). Under the stimulation of purely cold-hot cycles, all samples produced pyrophoric carriers. Among them, the BOI-N_{0.3} sample has the largest pyrophoric current density of 0.108 $\mu\text{A cm}^{-2}$ at 1.23 V vs. RHE, which is two times higher than that of BiOIO₃ (0.054 $\mu\text{A cm}^{-2}$ at 1.23 V vs. RHE) before modification. Combining with the I-T curves proves that the temperature change can increase the carrier density of the system. In addition, the overpotentials at current densities of 0.025 and 0.05 $\mu\text{A cm}^{-2}$ were compared in Fig. S6. Under cold-hot stimulation, the BOI-N_{0.3} electrode

only needs 0.475 V and 0.625 V overpotential to reach the above target potential, while the difference between the overpotential of BiOIO₃ electrode before and after is nearly two times. This indicates that the modified catalysts greatly improve the energy utilization efficiency. The carrier density was further increased by the introduction of the light field, and the final current density of BOI-N_{0.3} reached a maximum of 0.187 $\mu\text{A cm}^{-2}$ at 1.23 V vs. RHE, probably due to the subtle change in the structure of the IO₃ pyramid by the introduction of the N atom, which replaced the O at the V3 position and led to a change in the I-O bond length and thus promoted the pyroelectric polarization of BiOIO₃. Fig. 6(c) shows the J-V curves of BOI-N_{0.3} samples under different stimuli. As can be seen from the figure, the current density under the dual stimulation of light and cold-hot is higher than that of the hot or light field stimulation alone. The subsequent plotted ABPE curve shows the highest measured efficiency under combined light and temperature changes (Fig. S7), reaching 0.06% at 0.68 V vs. RHE. This indicates that the pyro-PEC system has a synergistic effect and is a reliable means to improve the catalytic effect. The carrier interfacial transfer efficiency of the catalysts was analyzed using electrochemical impedance spectroscopy. The corresponding equivalent circuit diagram is shown in Fig. S8. Herein, R₁ represents the ohmic resistance of the electrochemical process, C_{dl} is the double layer capacitor, R_{ct} means the charge transfer resistance at the interface between photoanode and electrolyte, Q is the constant-phase element, R₂ is the charge transfer resistance between Pt electrode and electrolyte. In general, the arc diameter is positively correlated with the R_{ct}[52]. The results show that BOI-N_{0.3} has the lowest interfacial transfer resistance. As shown in Fig. 6(f), the radii of impedance arcs under different environmental conditions of excitation are different. It is well known that a small impedance arc radius implies a small charge transfer potential inside the sample. The arc radius under both light and cold-hot excitation is smaller than all other conditions, which implies better interfacial transfer. This suggests that the pyro-PEC performance of BiOIO₃ is superior to the pyroelectric or photoelectric performance alone.

To investigate more visually the reason for the high catalytic activity of the BOI-N_{0.3} sample, a surface photovoltage spectrum (SPV) was obtained under heated conditions. The excitation of the semiconductor leads to a change in the surface potential distribution, so the potential change of the catalyst can be captured with this test. As shown in Fig. 7, the signal values detected for the samples after the introduction of N atoms are all higher than those of the pure BiOIO₃ samples, while the potential signal of BOI-N_{0.3} is much higher than that of the other samples. This may be caused by the change in I-O bonding after N replacement of O which enhances the polarization intensity of the

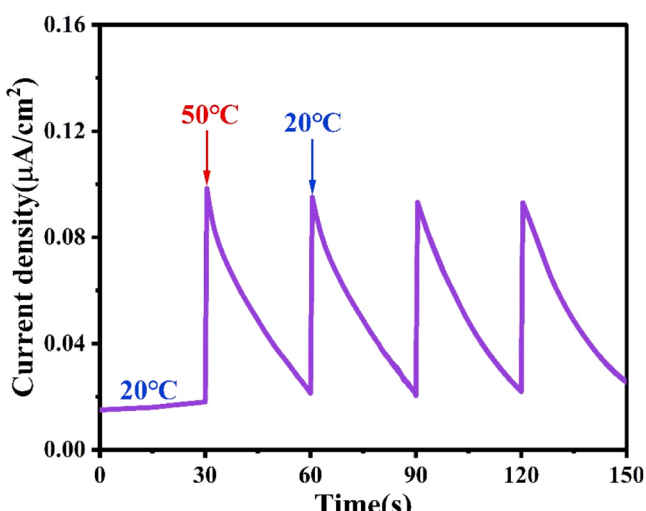


Fig. 5. Transient current density versus time (I-T) curve conducted at 1.23 V vs. RHE under cold-hot (20 °C – 50 °C) cycle excitations.

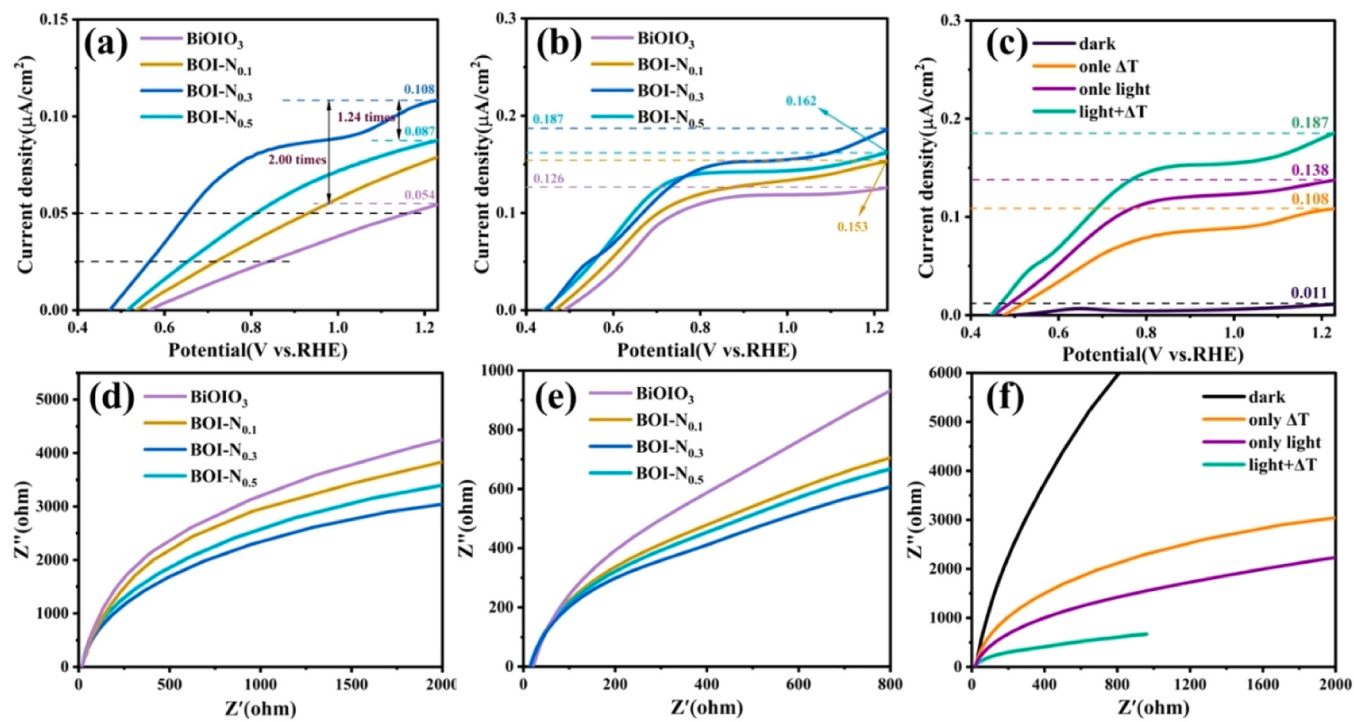


Fig. 6. Current density versus applied potential (J-V) curves of BiOIO₃ and BOI-N_x ($0.1 \leq x \leq 0.5$) samples. (a) only ΔT ; (b) light + ΔT ; (c) LSV curves of B1 sample under different environments; EIS Nyquist plots of BiOIO₃ and BOI-N_x ($0.1 \leq x \leq 0.5$) samples (d) only ΔT ; (e) light + ΔT ; (f) EIS curves of BOI-N_{0.3} sample under different environments.

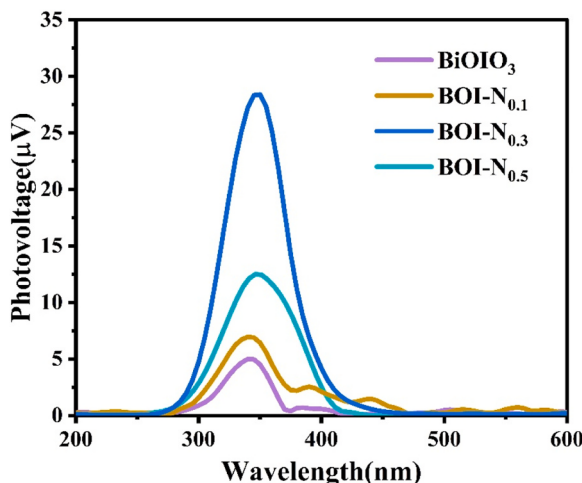


Fig. 7. Surface photovoltage (SPV) spectra of BiOIO₃ and BOI-N_x ($0.1 \leq x \leq 0.5$) samples.

samples. In addition, all samples show positive response signals, indicating the n-type semiconductor properties of the samples. That is, most of the carriers of BiOIO₃ are electrons, but the main carriers on the surface of the samples are holes. It also shows that the BOI-N_{0.3} samples have excellent carrier separation efficiency.

To further explore the effect of N introduction on the pyro-PEC performance of the samples and to better understand the charge transfer behavior during the catalytic process, we tested the Mott Schottky (M-S) curves of the BiOIO₃ samples and BOI-N_{0.3} samples under different catalytic environments. As shown in Fig. 8, all the curves show positive slope, indicating that the n-type properties of the semiconductor do not change before and after the modification, which is consistent with the analytical results of SPV. Comparing before and after the modification, it

can be found that the slope of the curves of the modified samples is significantly lower than that before the modification, which indicates that the carrier density increases significantly after the modification. At the same time, the carrier density is much larger when light and temperature changes are present at the same time than other conditions. Combining with the previous analysis, it can be inferred that pyro-PEC can significantly increase the carrier density. Besides, the V_{fb} values of different catalytic conditions were compared by extrapolating the images to $1 \text{ C}^{-2} = 0$ and summarized in Table 3. The results show that the modified samples have more negative V_{fb} values under the effect of temperature change. In other words, the modified samples have a greater degree of energy band bending in the catalytic process, and the holes can be more easily transferred to the catalyst surface and participate in the water splitting system. This can be explained by the fact that the introduction of N enhances the polarization of the catalyst and thus generates additional pyroelectric carriers, and the polarization electric field generated by the polarization optimizes the carrier transport kinetics. The above statement is supported by the fact that a larger energy band bending is generated when light and temperature changes act simultaneously. Subsequently, we performed structural optimization of BiOIO₃ and BOI-N_{0.3} using DFT calculations, and the results are shown in Fig. 9. The N atom replaced the O atom at the V3 position, and the replaced BiOIO₃ still maintained the dominant structure of the layers, so the morphology of the sample did not change significantly, which is consistent with the SEM images and TEM images. It is noteworthy that the introduction of N caused a change in the bond length of the I-O bond and the bond angle of O₃(N)-I-O₂. The bond length changed from 1.813 Å before modification to 2.031 Å after modification, and the bond angle changed from 91.794° to 86.748°. Because the pyroelectricity of BiOIO₃ originates from the asymmetric arrangement of IO₃ pyramids, combined with the previous discussion, the enhanced pyroelectricity and thermal photocatalytic properties of the modified samples may be attributed to the enhanced polarization caused by the change of IO₃ pyramids.

Fig. 10 summarizes the basic mechanism of the enhanced pyro-PEC

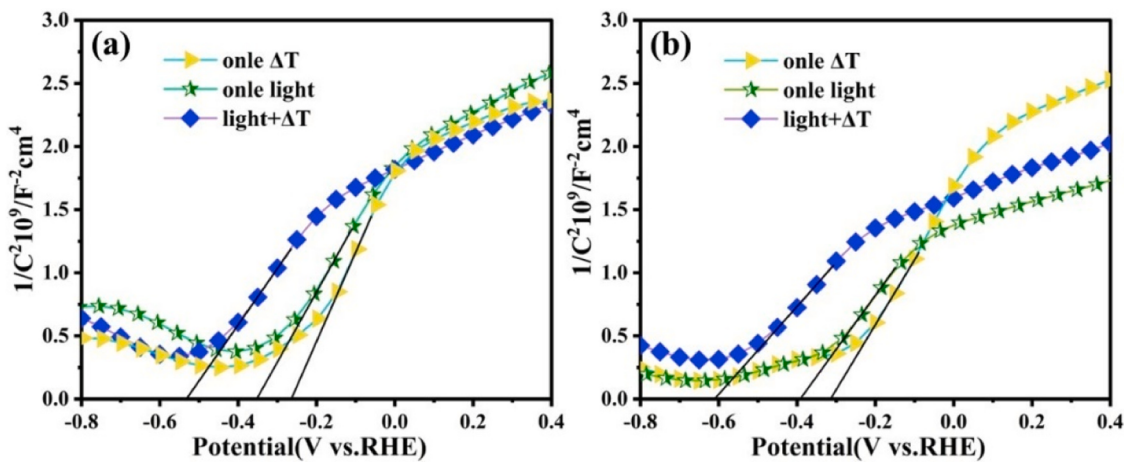


Fig. 8. Mott-Schottky plots collected at a fixed frequency of 1 kHz. (a) BiOIO_3 ; (b) $\text{BOI-N}_{0.3}$.

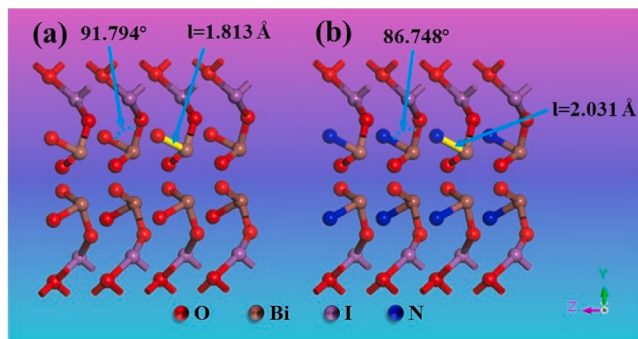


Fig. 9. The calculated crystal structures, the bond angles of $\text{O}_3(\text{N})-\text{I}-\text{O}_2$ and the lengths of the $\text{I}-\text{O}(\text{N})$ bonds were obtained. (a) BiOIO_3 ; (b) $\text{BOI-N}_{0.3}$.

performance by polarization after N introduction. For BiOIO_3 , the change in external temperature causes a change in the amplitude of the oscillation of the electric dipole moment inside the material. When the material undergoes spontaneous polarization, polarization charges are generated on both sides of the polarization direction, and the

polarization charges migrate to the material surface to participate in the redox reaction under the action of the polarization electric field. As the polarization proceeds, the polarization charges generated reach thermodynamic equilibrium and form a charge shield. $\Delta T > 0$, the polarization amplitude of the material decreases leading to the disruption of the original equilibrium, allowing the release of the excess compensating charges. $\Delta T < 0$, the polarization amplitude is enhanced and then the same result is achieved. The IO_3 polar group I-O bond length and the bond angle of $\text{O}_3(\text{N})-\text{I}-\text{O}_2$ were changed after the introduction of N. This enhances the pyroelectric polarization of BiOIO_3 , allowing more polarized charges to be released and participate in the reaction, ultimately improving the pyro-PEC performance. In addition, the redistribution of the polarization charge changes the degree of energy band bending, which enhances the polarization electric field to some extent and facilitates the carrier separation.

4. Conclusion

In summary, BiOIO_3 catalysts were prepared by a simple hydrothermal method. The urea and BiOIO_3 powders were annealed and treated to successfully introduce the element N into the lattice of the sample. Structural optimization showed that N replaced O at the V3

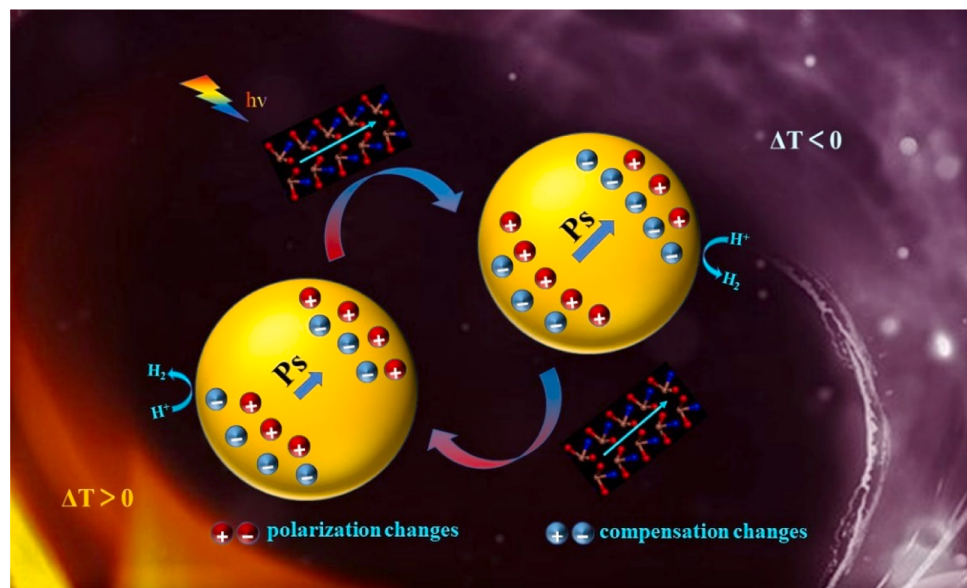


Fig. 10. Mechanism of polarization enhancement on the pyro-PEC polarization process after the introduction of N and the charge movement under cold-hot cycle.

position shifting the atomic occupancy of the IO_3 pyramid. This not only enhances the pyroelectric polarization, but also amplifies the effect of the polarized electric field, which provides the driving force for charge transport. As a result, the current density of the $\text{BOI-N}_{0.3}$ sample under temperature change excitation reaches $0.108 \mu\text{A cm}^{-2}$ at 1.23 V vs. RHE, which is twice as high as that of bare BiOIO_3 . The current density after introduction of light was further improved and reached the experimental maximum of $0.187 \mu\text{A cm}^{-2}$ at 1.23 V vs. RHE. This was attributed to the high pyro-PEC efficiency and the enhanced polarization. Pyro-photo-electrochemical tests, SPV tests and structural optimization confirm that the change in the position of the IO_3 polar group enhances the polarization properties and intensifies the internal polarization field, promoting carrier separation. This work provides a reference for further studies of polar groups in polar samples. In addition, it also provides inspiration for studying the relationship between the polarization electric field generated by pyroelectric polarization and PEC performance.

CRediT authorship contribution statement

Zhifeng Liu and Yunfei Wu conceived and designed the study. **Yunfei Wu, Mengnan Ruan and Chengyi Wang** performed the experiments. **Zhifeng Liu, Yunfei Wu, Mengnan Ruan, Zhengang Guo and Chengyi Wang** wrote the paper. **Zhifeng Liu, Yunfei Wu, Mengnan Ruan, Zhengang Guo and Chengyi Wang** reviewed and edited the manuscript. All authors read and approved the manuscript.

Declaration of Competing Interest

There are no conflicts of interest.

Data Availability

Data will be made available on request.

Acknowledgements

The authors gratefully acknowledge financial support from National Natural Science Foundation of China (No. 52073200).

Supporting Information

Supporting Information Experimental illustration, XPS, STEM-EDX and ABPE of $\text{BOI-N}_{0.3}$, FTIR, SEM and overpotential of BiOIO_3 and BOI-N_x ($0.1 \leq x \leq 0.5$), the ideal temperature curve, equivalent circuit diagram of electrochemical impedance, more calculation and XRD refinement details and flat band potential details (PDF).

Appendix A. Supporting information

Supplementary data associated with this article can be found in the online version at [doi:10.1016/j.apcatb.2023.123169](https://doi.org/10.1016/j.apcatb.2023.123169).

References

- K.T. Gillingham, C.R. Knittel, J. Li, M. Ovaere, M. Reguant, The short-run and long-run effects of Covid-19 on energy and the environment, Joule 4 (2020) 1337–1341.
- K. Dang, H. Dong, L. Wang, M. Jiang, S. Jiang, W. Sun, D. Wang, Y. Tian, Boosting electrochemical styrene transformation via tandem water oxidation over a single-atom $\text{Cr}_1/\text{CoSe}_2$ catalyst, Adv. Mater. 34 (2022) 2200302.
- Z. Li, Q. Zhang, J. Li, H. Sun, M. Yuen, S. Jiang, Y. Tian, G. Hong, C. Wang, M. Liu, Promoting photocatalytic hydrogen evolution over the perovskite oxide $\text{Pr}_{0.5}(\text{Ba}_{0.5}\text{Sr}_{0.5})_0.5\text{Co}_{0.8}\text{Fe}_{0.2}\text{O}_3$ by plasmon-induced hot electron injection, Nanoscale 12 (2020) 18710–18720.
- X. Wang, Y. Wang, Y. Wu, Y. Fan, Y. Tian, Dual-interlayers constructed by $\text{Ti}_3\text{C}_2\text{T}$ /ionic-liquid for enhanced performance of solid garnet batteries, J. Energy Chem. 78 (2023) 47–55.
- T. Yao, X. An, H. Han, J. Chen, C. Li, Photoelectrocatalytic materials for solar water splitting, Adv. Energy Mater. 8 (2018) 1800210.
- J. Zhang, C.Y. Toe, P. Kumar, J. Scott, R. Amal, Engineering defects in TiO_2 for the simultaneous production of hydrogen and organic products, Appl. Catal. B: Environ. 333 (2023), 122765.
- X. Zhang, C. Xu, L. Zhang, Z. Li, J. Hong, Y. Zhang, Photothermal catalytic water splitting at diverse two-phase interfaces based on Cu-TiO_2 , ACS Appl. Energy Mater. 5 (2022) 4564–4576.
- G.O. Rabell, M.R.A. Cruz, I. Juárez-Ramírez, Hydrogen production of ZnO and ZnO/Ag films by photocatalysis and photoelectrocatalysis, Mater. Sci. Semicond. Process. 134 (2021), 105985.
- K.H. Saini B, D. Laishram, R. Krishnapriya, R. Singhal, R.K. Sharma, Role of ZnO in ZnO Nanoflake/ Ti_3C_2 MXene composites in photocatalytic and electrocatalytic hydrogen evolution, ACS Appl. Nano Mater. 5 (2022) 9319–9333.
- F. Niu, Q. Zhou, R. Liu, K. Hu, Photoinduced hole hopping across CdS quantum dot surfaces for photoelectrochemical water oxidation, ACS Appl. Energy Mater. 5 (2022) 1244–1251.
- M. Zhang, S. Nie, T. Cheng, Y. Feng, C. Zhang, L. Zheng, L. Wu, W. Hao, Y. Ding, Enhancing the macroscopic polarization of CdS for piezo-photocatalytic water splitting, Nano Energy 90 (2021), 106635.
- H. Chai, L. Gao, P. Wang, F. Li, G. Hu, J. Jin, $\text{In}_2\text{S}_3/\text{F-Fe}_2\text{O}_3$ type-II heterojunction bonded by interfacial S-O for enhanced charge separation and transport in photoelectrochemical water oxidation, Appl. Catal. B: Environ. 305 (2022), 121011.
- P. Wang, S. Wang, L. Gao, X. Long, H. Chai, F. Li, Q. Wang, J. Jin, Achieving surface-sealing of hematite nanoarray photoanode with controllable metal-organic frameworks shell for enhanced photoelectrochemical water oxidation, J. Catal. 413 (2022) 398–406.
- K. Tian, L. Wu, H. Chai, L. Gao, M. Wang, H. Niu, L. Chen, J. Jin, Enhancement of charge separation and hole utilization in a $\text{Ni}_2\text{P}_2\text{O}_7$ -nd- BiVO_4 photoanode for efficient photoelectrochemical water oxidation, J. Colloid Interface Sci. 644 (2023) 124–133.
- K. Tian, L. Wu, T. Han, L. Gao, P. Wang, H. Chai, J. Jin, Dual modification of BiVO_4 photoanode by rare earth element neodymium doping and further NiFe_2O_4 co-catalyst deposition for efficient photoelectrochemical water oxidation, J. Alloy. Compd. 923 (2022), 166352.
- C. Lai, J. Chen, J. Chang, C. Kuo, Y. Liu, J. Yang, Y.T. Hsieh, S.W. Tseng, Y.C. Pu, Two-step process of a crystal facet-modulated BiVO_4 photoanode for efficiency improvement in photoelectrochemical hydrogen evolution, ACS Appl. Mater. Interfaces 14 (2022) 24919–24928.
- K. Dang, S. Zhang, X. Wang, W. Sun, L. Wang, Y. Tian, S. Zhan, Cobalt diselenide (001) surface with short-range Co-Co interaction triggering high-performance electrocatalytic oxygen evolution, Nano Res. 14 (2021) 4848–4856.
- H. Zhang, J.S. Lee, Hybrid microwave annealing synthesizes highly crystalline nanostructures for (photo)electrocatalytic water splitting, Acc. Chem. Res. 52 (2019) 3132–3142.
- X. Wang, W. Sun, Y. Tian, K. Dang, Q. Zhang, Z. Shen, S. Zhan, Conjugated π electrons of MOFs drive charge separation at heterostructures interface for enhanced photoelectrochemical water oxidation, Small 17 (2021) 2100367.
- Y. Zhu, J. Chen, L. Shao, X. Xia, Y. Liu, L. Wang, Oriented facet heterojunctions on CdS nanowires with high photoactivity and photostability for water splitting, Appl. Catal. B: Environ. 268 (2020), 118744.
- G. Zheng, J. Wang, G. Zu, H. Che, C. Lai, H. Li, V. Murugadoss, C. Yan, J. Fan, Z. Guo, Sandwich structured WO_3 nanoplatelets for highly efficient photoelectrochemical water splitting, J. Mater. Chem. A 7 (2019) 26077–26088.
- T. Han, L. Wu, M. Wang, L. Gao, X. Long, J. Liang, B. Yang, J. Jin, A novel co-catalyst of CoFeOOH for greatly improving the solar water splitting performance over Mo-doped bismuth vanadate, J. Alloy. Compd. 932 (2023), 167633.
- J. Kang, K.-Y. Yoon, J.-E. Lee, J. Park, S. Chaule, J.-H. Jang, Meso-pore generating P doping for efficient photoelectrochemical water splitting, Nano Energy 107 (2023), 108090.
- X. Zhao, K. Tang, X. Wang, W. Qi, H. Yu, C.-F. Du, Q. Ye, A self-supported bifunctional MoNi_3 framework with iron doping for ultra-efficient water splitting, J. Mater. Chem. A 11 (2023) 3408–3417.
- Y. Li, C. Gao, W. Jiang, C. Zhuang, W. Tan, W. Li, Y. Li, L. Wang, X. Liao, Z. Sun, J. Zou, X. Han, A game-changing design of low-cost, large-size porous cocatalysts decorated by ultra-small photocatalysts for highly efficient hydrogen evolution, Appl. Catal. B: Environ. 286 (2021), 119923.
- V. Nair, M.J. Munoz-Batista, M. Fernandez-Garcia, R. Luque, J.C. Colmenares, Thermo-photocatalysis: environmental and energy applications, ChemSusChem 12 (2019) 2098–2116.
- H. He, X. Lu, E. Hanc, C. Chen, H. Zhang, L. Lu, Advances in lead-free pyroelectric materials: a comprehensive review, J. Mater. Chem. C. 8 (2020) 1494–1516.
- H. You, S. Li, Y. Fan, X. Guo, Z. Lin, R. Ding, X. Cheng, H. Zhang, T.W.B. Lo, J. Hao, Y. Zhu, H.Y. Tam, D. Lei, C.H. Lam, H. Huang, Accelerated pyro-catalytic hydrogen production enabled by plasmonic local heating of au on pyroelectric BaTiO_3 nanoparticles, Nat. Commun. 13 (2022) 6144.
- M. Swaisi, A. Dorfler, R. Katoch, A. Ruediger, Smooth pyroelectric luminescence in LiNbO_3 single crystals, J. Phys.: Condens. Matter 32 (2020), 295701.
- Z. Qiao, Z. Liu, M. Ruan, Z. Guo, W. Yan, X. Wu, Thermal excitation polarized field drives photoelectric catalysis for dye degradation in a $\text{BaTiO}_3/\text{CdS}$ heterojunction through integration of solar and thermal energy, ChemPhotoChem 5 (2021) 1106–1118.
- Z. Li, G. Huang, Y. Wang, C. Lu, H. Huang, J. Kou, Pyroelectric effects in CdS phase junctions for dual-enhanced photocatalytic hydrogen production, Catal. Sci. Technol. 13 (2023) 2559–2565.

[32] M. Zhang, Q. Hu, K. Ma, Y. Ding, C. Li, Pyroelectric effect in CdS nanorods decorated with a molecular co-catalyst for hydrogen evolution, *Nano Energy* 73 (2020), 104810.

[33] X. Dong, G. Yao, Q. Liu, Q. Zhao, Z. Zhao, Spontaneous polarization effect and photocatalytic activity of layered compound of BiO_3 , *Inorg. Chem.* 58 (2019) 15344–15353.

[34] M. Zhang, L. Fulanović, S. Egert, H. Ding, P.B. Groszewicz, H.-J. Kleebe, L. Molina-Luna, J. Koruza, Electric-field-induced antiferroelectric to ferroelectric phase transition in polycrystalline NaNb_3 , *Acta Mater.* 200 (2020) 127–135.

[35] T. Li, Z. Liu, Y. Meng, Two-dimensional ultra-thin nanosheets optimize the surface reaction dynamics and photo/pyro-generated carrier transfer of NaNb_3 for an efficient pyro-photo-electric catalytic system, *Sustain. Energy Fuels* 6 (2022) 4227–4239.

[36] S.D. Nguyen, J. Yeon, S.H. Kim, P.S. Halasyamani, A. $\text{BiO}(\text{IO}_3)$, new polar iodate that exhibits an Aurivillius-type $(\text{Bi}_2\text{O}_2)^{2+}$ layer and a large SHG response, *J. Am. Chem. Soc.* 133 (2011) 12422–12425.

[37] Y. Su, L. Zhang, W. Wang, Internal polar field enhanced H_2 evolution of BiOIO_3 nanoplates, *Int. J. Hydrom. Energy* 41 (2016) 10170–10177.

[38] J. Yang, D. Zheng, X. Xiao, X. Wu, X. Zuo, J. Nan, Iodine self-doping and oxygen vacancies doubly surface-modified BiOIO_3 : Facile in situ synthesis, band gap modulation, and excellent visible-light photocatalytic activity, *Chem. Eng. J.* 373 (2019) 935–945.

[39] J. You, Z. Liu, Z. Guo, M. Ruan, W. Yan, Doping of W ions to modulate the polarization intensity of Bi_2WO_6 for efficient piezoelectric-photoelectrochemical water splitting, *ACS Appl. Energy Mater.* 5 (2022) 11472–11482.

[40] Y. Liu, Q. Li, Z. Lian, J. Fan, Y. Tao, G. Li, H. Li, Polarization field promoted photoelectrocatalysis for synergistic environmental remediation and H_2 production, *Chem. Eng. J.* 437 (2022), 135132.

[41] M. Zargazi, M.H. Entezari, Ultrasound assisted deposition of highly stable self-assembled Bi_2MoO_6 nanoplates with selective crystal facet engineering as photoanode, *Ultrason. Sonochem.* 67 (2020), 105145.

[42] M. Lu, X. Xiao, G. Zeng, Bi_2S_3 nanorods and BiOI nanosheets co-modified BiOIO_3 nanosheets: an efficient vis-light response photocatalysts for RhB degradation, *J. Alloy. Compd.* 885 (2021), 160996.

[43] J. Xu, W. Li, W. Liu, J. Jing, K. Zhang, L. Liu, J. Yang, E. Zhu, J. Li, Y. Zhu, Efficient photocatalytic hydrogen and oxygen evolution by side-group engineered benzodimidazole oligomers with strong built-in electric fields and short-range crystallinity, *Angew. Chem. Int. Ed.* 61 (2022), e202212243.

[44] H. Su, S. Li, L. Xu, C. Liu, R. Zhang, W. Tan, Hydrothermal preparation of flower-like Ni^{2+} doped Bi_2WO_6 for enhanced photocatalytic degradation, *J. Phys. Chem. Solids* 170 (2022), 110954.

[45] X. Hu, R. Guo, Z. Lin, Z. Bi, X. Chen, J. Wang, W. Pan, Construction of carbon dot-modified $\text{g-C}_3\text{N}_4/\text{BiOIO}_3$ z-scheme heterojunction for boosting photocatalytic CO_2 reduction under full spectrum light, *ACS Sustain. Chem. Eng.* 10 (2022) 11143–11153.

[46] J. Guo, J. Wu, Y. Guan, J. Wang, Q. Liu, X. Mao, X. Qi, P. He, H. Wang, Fabrication of a z-scheme heterojunction polyhedral-shaped $\text{BiOIO}_3/\text{MIL}-53(\text{Fe})$ photocatalyst for enhancing gaseous Hg^0 removal, *Energy Fuels* 35 (2021) 3252–3265.

[47] L. Kan, C. Chang, Q. Wang, X. Wang, Glycol assisted splitting BiOIO_3 into plasmonic bismuth coupled with BiOI co-modified Bi_2WO_6 ($\text{BiOI/Bi/Bi}_2\text{WO}_6$) to form indirect z-scheme heterojunction for efficient photocatalytic degradation of BPA, *Sep. Purif. Technol.* 297 (2022), 121537.

[48] X. Kong, Z. Peng, R. Jiang, P. Jia, J. Feng, P. Yang, Q. Chi, W. Ye, F. Xu, P. Gao, Nanolayered heterostructures of N-doped TiO_2 and N-doped carbon for hydrogen evolution, *ACS Appl. Nano Mater.* 3 (2020) 1373–1381.

[49] H. Zhang, C. Niu, S. Yang, G. Zeng, Facile fabrication of $\text{BiOIO}_3/\text{BiOBr}$ composites with enhanced visible light photocatalytic activity, *RSC Adv.* 6 (2016) 64617–64625.

[50] H. Huang, H. Ou, J. Feng, X. Du, Y. Zhang, Achieving highly promoted visible-light sensitive photocatalytic activity on BiOIO_3 via facile iodine doping, *Colloids Surf. A: Physicochem. Eng. Asp.* 518 (2017) 158–165.

[51] T. Jia, J. Wu, J. Song, Q. Liu, J. Wang, Y. Qi, P. He, X. Qi, L. Yang, P. Zhao, In situ self-growing 3D hierarchical BiOBr/BiOIO_3 z-scheme heterojunction with rich oxygen vacancies and iodine ions as carriers transfer dual-channels for enhanced photocatalytic activity, *Chem. Eng. J.* 396 (2020), 125258.

[52] F. Chen, Z. Ma, L. Ye, T. Ma, T. Zhang, Y. Zhang, H. Huang, Macroscopic spontaneous polarization and surface oxygen vacancies collaboratively boosting CO_2 photoreduction on BiOIO_3 single crystals, *Adv. Mater.* 32 (2020) 1908350.